

POLYNOMIAL APODIZERS FOR CENTRALLY OBSCURED VORTEX CORONAGRAPHS

KEVIN FOGARTY¹, LAURENT PUEYO², JOHAN MAZOYER^{1, 2}, MAMADOU N'DIAYE^{3, 2}

Submitted to the *Astrophysical Journal*

ABSTRACT

Several coronagraph designs have been proposed over the last two decades to directly image exoplanets. Among these designs, the vector vortex coronagraphs provide theoretically perfect starlight cancellation along with small inner working angles when deployed on telescopes with unobstructed pupils. However, current and planned space missions and ground-based extremely large telescopes present complex pupil geometries, including secondary mirror central obscurations, that prevent vortex coronagraphs from rejecting on-axis sources entirely. Recent solutions combining the vortex phase mask with a ring-apodized pupil have been proposed to circumvent this issue, but provide a limited throughput for vortex charges > 2 . We present a family of pupil plane apodizations that compensate for pupil geometries with circularly symmetric central obstructions caused by on-axis secondary mirrors for charge 2, 4, and 6 vector vortex coronagraphs. These apodizations are derived analytically and allow the vortex coronagraph to retain theoretically perfect nulling in the presence of central obscurations. For a charge 4 vortex, we design polynomial apodization functions assuming a greyscale apodizing filter that represent a substantial gain in throughput over the ring-apodized vortex coronagraph design, while for a charge 6 vortex, we design polynomial apodized vortex coronagraphs that have $\gtrsim 70\%$ total energy throughput for the entire range of central obscuration sizes studied. We propose methods for optimizing apodizations produced with either greyscale apodizing filters or shaped mirrors. We conclude by demonstrating how this design may be combined with apodizations numerically optimized for struts and segment gaps in telescope pupils to design terrestrial exoplanet imagers for complex pupils.

Subject headings: planets and satellites: detection - instrumentation: adaptive optics - instrumentation: high angular resolution - techniques: high angular resolution - telescopes

1. INTRODUCTION

Upcoming and proposed large ground and space-based telescope designs offer the sensitivity and resolution necessary to begin probing sub-Jovian and, in the case of space missions, eventually terrestrial exoplanets with high contrast direct imaging (Kasper et al. 2010; Bolcar et al. 2015; Dalcanton et al. 2015). High contrast imaging with coronagraphic instruments has been recently successful directly imaging protoplanetary discs and massive, young exoplanets (Marois et al. 2008; Kalas et al. 2008; Lagrange et al. 2009; Marois et al. 2010; Andrews et al. 2011; Carson et al. 2013; Kuzuhara et al. 2013; Rameau et al. 2013; Mancini et al. 2015; Macintosh et al. 2015; Wagner et al. 2015). However, maximizing the usefulness of future observatories poses a challenge for coronagraph designs, since instrument designs developed to directly image Earth-like exoplanets will need to be adapted for obstructed pupil geometries (Pueyo & Norman 2013; Soummer et al. 2011; Guyon et al. 2014).

Significant effort has been directed towards coronagraphic concepts proposed for directly imaging exoplanets with telescopes with obstructed pupils. Using one approach, the original Lyot coronagraph design can be modified by altering the shape of the Lyot stop to block artifacts introduced by the pupil geometry in the Lyot plane (Sivaramakrishnan et al. 2001; Sivaramakrishnan & Yaitskova 2005). Other approaches involve a com-

bination of modifications to the pupil and focal plane geometries of the coronagraph, both to improve coronagraphic performance for unobstructed pupils and to compensate for complicated pupils. For example, the apodized pupil Lyot coronagraph (APLC) modifies the Lyot coronagraph by introducing a pupil apodizing mask in order to improve starlight suppression for broadband light with an obstructed pupil (Soummer 2005; N'Diaye et al. 2015). Phase Induced Amplitude Apodization (PIAA) of the pupil plane with shaped mirrors, combined with a system of apodizers and inverse-optics, has also been widely explored as a method for overcoming arbitrary pupil shapes (Guyon 2003; Traub & Vanderbei 2003; Guyon et al. 2005; Cady 2012). Active Correction of Aperture Discontinuities (ACAD) has been proposed as a method for using deformable mirrors to mitigate diffraction due to the discontinuities imposed on the pupil by secondary struts and primary mirror gaps in order to improve the performance of coronagraphic designs it is coupled with (Pueyo & Norman 2013). Meanwhile, coronagraph designs that replace the conventional occulting spot in the focal plane of a Lyot coronagraph with more complex masks that involve a combination of phase shifting and apodization have been introduced, such as the hybrid Lyot coronagraph and coronagraphs designed to use the four quadrant phase mask (Rouan et al. 2000; Kuchner & Traub 2002; Murakami & Baba 2005; Moody & Trauger 2007; Moody et al. 2008; Trauger et al. 2012). Fixed mirror apodization techniques have been combined with these more complex coronagraph designs, such as the PIAA complex mask coronagraph (PI-

¹ Department of Physics and Astronomy, Johns Hopkins University, Baltimore, USA

² Space Telescope Science Institute, Baltimore, USA

³ Observatoire de la Côte d'Azur, Nice, France

AACMC) (Guyon et al. 2014). These recent instrument designs depart considerably from the coronagraph proposed in Lyot (1939), and represent substantial progress towards achieving terrestrial exoplanet direct imaging capability.

Coronagraphs using a vector vortex phase mask in the focal plane potentially provide substantial gains over other designs in starlight suppression while maintaining high instrumental throughput for sources at close separations from a target star (Foo et al. 2005; Mawet et al. 2005). A vortex phase mask of charge c functions by introducing a phase term $e^{ic\theta}$ to the electric field in the focal plane, where θ is the angular coordinate in the focal plane. The vortex phase mask in principle provides full cancellation of on-axis starlight with little suppression nearby off-axis sources (Mawet et al. 2011a). Charge 2 vortex coronagraphs also permit small, $\sim 1\lambda/D$ inner working angles (IWAs), at the expense of sensitivity to low-order aberrations and finite stellar angular size (Mawet et al. 2009, 2011b). Vortex coronagraphs charge of 4 or even 6, which trade-off higher stability for a larger IWA, are typically considered more likely candidates for exoplanet characterizing instruments (Jenkins 2008; Mawet et al. 2010). However, the main limitation to using a vortex coronagraph with a telescope with a complicated pupil geometry is the loss of starlight suppression induced by pupil obstructions, and in particular the central obstruction of on-axis telescopes. In the absence of pupil obstructions they are theoretically ‘perfect’ coronagraphs, since in addition to entirely rejecting the light from the target star, they are theoretically intrinsically achromatic owing to their phase-only geometry in the focal plane (Mawet et al. 2005, 2007).

Recent work has made progress towards adapting the vortex coronagraph for on-axis telescopes and telescopes with struts and gaps obstructing the pupil. Mawet et al. (2013) has proposed an analytical solution to the problem of the central obscuration, by apodizing the pupil with a filter consisting of semi-transmissive, hard edged annuli or ‘rings’. The ring apodized vortex coronagraph (RAVC) solves the issue of the artifact from the central obscuration imposed by a secondary mirror, which is the largest cause of pupil-geometry induced stellar flux residual in the coronagraphic image.

Unfortunately, the throughput of the RAVC decreases rapidly both as the charge of the vortex mask and as the radius of the central obscuration increases. For this reason, the RAVC is an appealing method for correcting for the central obscuration with a charge 2 vortex coronagraph, but not for higher charges. Charge 2 vortex coronagraphs are suitable for instruments designed to achieve contrasts of $\sim 10^{-6}$; however, the sensitivity of the charge 2 vortex phase mask to low-order aberrations prevents it from being useful for obtaining larger contrasts (Mawet et al. 2010). Addressing applications which require much higher contrasts, such as terrestrial exoplanet imaging, with a vortex coronagraph requires use of higher charge vortices. Therefore, we seek alternatives to the RAVC for high-contrast imaging applications with on-axis telescopes.

In this paper we present an analytical method to compensate for the central obscuration of an on-axis telescope with a vortex coronagraph. Our results are a gen-

eralization of the RAVC, obtained by using a polynomial approach to extend the formalism of previous work presented in Fogarty et al. (2014) and derive novel solutions. Our previous work addresses the issue of limited throughput provided by the charge 4 RAVC, by finding an apodized vortex coronagraph that can provide 10^{-10} monochromatic starlight suppression and relatively high (31%) throughput for a telescope with a secondary mirror radius 30% of the primary mirror radius. We adopt the linear programming formalism used in that paper to optimize pupil apodizations composed of a set of functions, which in the case of the present paper are piecewise polynomials. Unlike in the previous paper, we use this formalism to find a family of throughput-maximizing pupil plane apodizations for charge 2, 4, and 6 vector vortex coronagraphs that produce theoretically perfect cancellation of on-axis starlight.

The polynomial apodized vortex coronagraph (PAVC) designs we describe in this paper have several desirable properties that make them a good candidate for delivering extremely high contrast imaging on large, on-axis telescopes. Like the RAVC, PAVC designs are inherently broadband and offer an exact solution to the problem posed by centrally obscured pupils. However, the throughput of a PAVC increases as the charge of the vortex increases. Throughput also falls as a function of secondary mirror radius more gradually than the RAVC for charges > 2 . As a result, the charge 4 and 6 PAVC are viable options for designing a coronagraph on a telescope with a large central obscuration.

We show that the terms in the piecewise polynomial description of a PAVC apodization produce electric field amplitudes that can be described analytically in the Lyot plane of a vortex coronagraph. We demonstrate how these terms can be arranged to produce an annulus of 0 electric field amplitude in the Lyot ring. Taking advantage of the large number of possible solutions available that null the Lyot plane electric field (PAVC apodizations have a large number of degrees of freedom, and can be either discontinuous or smooth), we present charge 2, 4, and 6 PAVCs that are optimized to maximize transmission if the pupil apodization is produced by an apodizing filter. We also present examples of apodization functions that may be produced by pairs of shaped mirrors, using a similar technique to PIAA, and that minimize the curvature of these mirrors.

This paper is divided into six sections. In § 2, we remind the reader of the definition of the vortex operator and derive analytical expressions that describe the behavior of the electric field of an on-axis source in the Lyot plane for a PAVC with a centrally obstructed pupil. In § 3, we use these results to set up the linear program that we will use to find apodizations that null the Lyot plane and optimize for a desired figure of merit. In § 4, we present apodization functions that are optimized to maximize transmission if we use a ‘classical’ apodizing mask to provide partial transmission through the telescope pupil, such as the microdot greyscale filter described in Martinez et al. (2009). In § 5, we calculate pairs of mirror shapes that produce apodizations for the charge 4 and 6 PAVC, present apodizations that minimize the mirrors’ curvature. In § 6, we discuss the applications of these results and also examine how the PAVC may be paired with other algorithms to optimize

contrast and throughput on telescopes with complicated pupil geometries. Finally, in § 7, we provide our concluding remarks.

2. THE CENTRALLY OBSCURED VORTEX OPERATOR

2.1. The Vortex Operator

We calculate the “vortex operator” mapping the electric field at the entrance pupil to the electric field in the Lyot plane for the PAVC setup depicted in Figure 1. We can use this operator to analytically describe the Lyot plane electric field of a vortex coronagraph apodized by a function consisting of the sum of piecewise polynomials. We can then constrain the coefficients of these polynomials to allow us to compute optimal PAVCs that have no on-axis source flux in the Lyot plane using linear programming.

The coronagraphic setup in Figure 1 consists of three stages: a pupil plane apodizer, depicted in Figure 1 as a grayscale apodizing filter (stage A), a vortex phase mask in the focal plane (stage B), and an inner Lyot stop (stage C). The inner Lyot stop blocks flux within a radius R_I in the Lyot plane. Light from a directly on-axis source enters a pupil with an obscuring secondary mirror of radius R_S . At stage A, the pupil is apodized with a filter. After being transformed to the focal plane, the light propagates through the vortex mask, at stage B. The apodizing filter is optimized such that at stage C, the electric field is exactly zero in the pupil at radii greater than R_I and less than the pupil radius R_P . At stage C, the beam hits the inner Lyot stop, resulting in a final image that exactly nulls the on-axis star.

The vortex operator for a vortex of charge c , $V_c[A(r)]$, maps the pupil apodization function $A(r)$ at Stage A to the electric field in the Lyot plane at stage C. To start with, the flux from a point source of unit intensity in the pupil of a telescope with a pupil radius R_P and a secondary-mirror induced central obscuration of radius R_S is

$$P(r) = \Pi_{0,R_P}(r) - \Pi_{0,R_S}(r), \quad (1)$$

$$\begin{aligned} V_c[A(r)] &= \int_0^\infty \left(\int_0^\infty A(r') (\Pi_{0,R_P}(r') - \Pi_{0,R_S}(r')) J_0(kr') r' dr' \right) J_c(kr) k dk \\ &= \int_0^\infty \left(\int_{R_S}^{R_P} A(r') J_0(kr') r' dr' \right) J_c(kr) k dk. \end{aligned} \quad (5)$$

2.2. Propagation of Polynomials

Since we are interested in finding a circularly symmetric analytical function for the pupil apodizing mask shape, whatever pupil mask geometry we end up with can be decomposed into terms r^n .¹ For even charges c , if $A(r) = r^n$ in Equation 5, then $V_c[r^n]$ is a piecewise

where $\Pi_{a,b}(x)$ is a unit boxcar function with lower bound a and upper bound b . For a given apodization $A(r)$, the apodized electric field at stage A, F_A is

$$F_A(r) = A(r) P(r). \quad (2)$$

At stage B, the beam undergoes a Fourier transformation, and is acted on by a vortex phase mask of charge c in the image plane. Since F_A is an axisymmetric function, the Fourier Transform of F_A is equivalent to the order-0 Hankel Transform. The field at stage B just before the vortex phase mask is therefore

$$F_B(k) = H_0[F_A(r)], \quad (3)$$

where r is the radial coordinate in the pupil plane and k is the radial coordinate in the image plane. After the beam passes through the vortex phase mask, the electric field is $F_B(k) e^{ic\theta}$. The flux is transformed back to the pupil plane at stage C. Just before the Lyot stop, the flux at stage C is $F_C(r) = H_c^{-1}[F_B(k)]$, where H_c^{-1} is the inverse Hankel transform of order c . This can be obtained by re-arranging the inverse Fourier transform:

$$\begin{aligned} F_C(r) &= \frac{1}{2\pi} \int F_B(k) e^{ic\theta} e^{i \sin kr \theta} k dk d\theta_k \\ &= \int_0^\infty F_B(k) \left(\frac{1}{2\pi} \int_{-\pi}^\pi e^{-i(c\tau - kr \sin \tau)} d\tau \right) k dk \\ &= \int_0^\infty F_B(k) J_c(kr) k dk \\ &= H_c^{-1}(F_B(k)), \end{aligned} \quad (4)$$

where J_c is the Bessel function of order c and where we have dropped the final phase term. Putting equations 3 and 4 together, we get the expression that maps F_A to F_C , which is the vortex operator V_c . Therefore, $V_c[A(r)] = H_c^{-1}[H_0[A(r)P(r)]]$. Expanding this out, we get,

polynomial expression. For $c = 2$,

$$V_2[r^n] = \begin{cases} 0, & \text{if } r < R_S \\ \frac{-n}{n+2} r^n + \frac{2}{n+2} R_S^{n+2} \frac{1}{r^2}, & \text{if } R_S \leq r \leq R_P \\ \frac{-2}{n+2} (R_S^{n+2} - R_P^{n+2}) \frac{1}{r^2}, & \text{if } r > R_P, \end{cases} \quad (6)$$

¹ A derivation of the propagation of non-circular pupil geometry terms can be found in Appendix A.

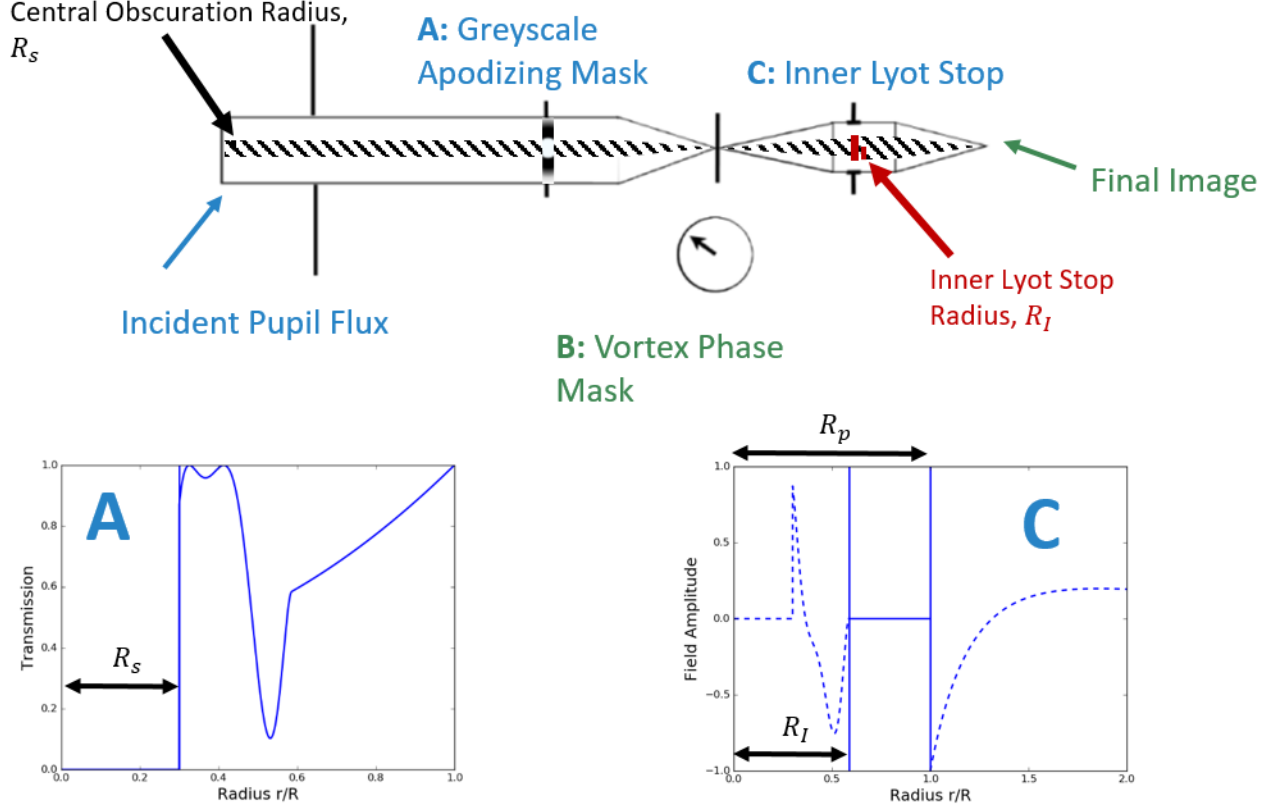


FIG. 1.— An overview of the coronagraphic setup discussed in this paper. The coronagraph consists of three stages: (A) the apodizing mask, (B) the vortex phase mask, and (C) the inner Lyot stop. When the beam hits stages A and C, it is in the pupil plane, and at stage B it is in the focal plane. The diagonal hatching indicates the region of the beam that is blocked by the secondary mirror and by the inner Lyot stop. In this figure, blue text refers to parts of the beam in the pupil plane, while green text refers to parts of the beam in the focal plane, including the final image PSF. The bottom left inset shows an example of the apodized transmission of flux from an on-axis source through stage A, with an apodization function optimized for a charge 4 vortex and a central obscuration that is 30% the radius of the pupil. The bottom right inset shows the field at stage C- the dashed lines show where the field is either outside the radius of the pupil R_P or is blocked by the inner Lyot stop with radius R_I .

for $c = 4$,

$$V_4[r^n] = \begin{cases} 0, & \text{if } r < R_S \\ \frac{(n-2)nr^n}{(n+2)(n+4)} - \frac{4R_S^{n+2}}{n+2} \frac{1}{r^2} & \text{if } R_S \leq r \leq R_P \\ + \frac{12R_S^{n+4}}{n+4} \frac{1}{r^4} & \\ - \frac{4(R_S^{n+2} - R_P^{n+2})}{n+2} \frac{1}{r^2} + & \text{if } r > R_P \\ \frac{12(R_S^{n+4} - R_P^{n+4})}{n+4} \frac{1}{r^4} & \end{cases} \quad (7)$$

and for $c = 6$,

$$V_6[r^n] = \begin{cases} 0, & \text{if } r < R_S \\ \frac{-n(n-2)(n-4)}{(n+2)(n+4)(n+6)} r^n + \frac{6R_S^{n+2}}{n+2} \frac{1}{r^2} & \text{if } R_S \leq r \leq R_P \\ - \frac{48R_S^{n+4}}{n+4} \frac{1}{r^4} + \frac{60R_S^{n+6}}{n+6} \frac{1}{r^6} & \\ \frac{6(R_S^{n+2} - R_P^{n+2})}{n+2} \frac{1}{r^2} - \frac{48(R_S^{n+4} - R_P^{n+4})}{n+4} \frac{1}{r^4} & \text{if } r > R_P \\ + \frac{60(R_S^{n+6} - R_P^{n+6})}{n+6} \frac{1}{r^6} & \end{cases} \quad (8)$$

For larger even charges, similar expressions of increasing length may be calculated.

3. OPTIMAL MASK ALGORITHM

In this section, we set up a linear program to find an apodizing mask of the form

$$A(r) = \begin{cases} \sum_{n=0}^N a_n r^n, & \text{if } R_S < r \leq R_I. \\ \sum_{n=0}^N a_n r^n + b_n r^n, & \text{if } R_I < r \leq R_P, \end{cases} \quad (9)$$

that produces 0 electric field in the Lyot plane between R_I and R_P , with $R_I \geq R_S$. Since the inner Lyot stop covers the region $r < R_I$ in the Lyot plane, an apodization function that is a solution to the linear program produces perfect cancellation of the on-axis starlight. We define the apodizing mask geometry with an N th order piecewise polynomial function. The b_n components of $A(r)$ are defined such that they are 0 at $r \leq R_I$. Therefore, when these components are acted on by the vortex operator in Equations 6, 7, or 8, R_S is replaced by R_I . This ensures that when we sum up the terms of $A(r)$ propagated into the Lyot plane, there exists a solution with 0 electric field at $R_I < r \leq R_P$. For the case of a charge 2 vortex, the criterion that $V_2[A(r)] = 0$ in $R_I < r \leq R_P$ translates to the linear constraints:

$$\sum_{n=0}^N \left(\frac{2R_S^{n+2}}{n+2} a_n + \frac{2R_I^{n+2}}{n+2} b_n \right) = 0, \quad (10a)$$

$$a_n + b_n = 0, \text{ if } n > 0. \quad (10b)$$

For a charge 4 vortex, the constraints are

$$\sum_{n=0}^N \left(-\frac{4R_S^{n+2}}{n+2} a_n - \frac{4R_I^{n+2}}{n+2} b_n \right) = 0, \quad (11a)$$

$$\sum_{n=0}^N \left(\frac{12R_S^{n+4}}{n+4} a_n - \frac{12R_I^{n+4}}{n+4} b_n \right) = 0, \quad (11b)$$

$$a_n + b_n = 0, \text{ if } n \neq (0, 2). \quad (11c)$$

For a charge 6 vortex, they are

$$\sum_{n=0}^N \left(\frac{6R_S^{n+2}}{n+2} a_n + \frac{6R_I^{n+2}}{n+2} b_n \right) = 0, \quad (12a)$$

$$\sum_{n=0}^N \left(-\frac{48R_S^{n+4}}{n+4} a_n - \frac{48R_I^{n+4}}{n+4} b_n \right) = 0, \quad (12b)$$

$$\sum_{n=0}^N \left(\frac{60R_S^{n+6}}{n+6} a_n + \frac{60R_I^{n+6}}{n+6} b_n \right) = 0, \quad (12c)$$

$$a_n + b_n = 0, \text{ if } n \neq (0, 2, 4). \quad (12d)$$

It is also necessary that the solution correspond to a physically real apodizing mask, which is guaranteed by the constraint

$$0 \leq A(r) \leq 1. \quad (13)$$

Since we would like to calculate mask shapes that can be produced using either a classical apodizer or a shaped mirror, we may desire mask shapes that are smooth. We constrain the mask shapes to be continuous, using

$$\sum_{n=0}^N b_n R_I^n = 0, \quad (14)$$

and smooth, using

$$\sum_{n=0}^N n b_n R_I^{n-1} = 0. \quad (15)$$

We are free to add degrees of freedom to the problem by increasing the order of the polynomials describing $A(r)$. Therefore, we can add similar linear constraints while ensuring that the problem remains solvable, and can for example ensure that the mask solution be C^k smooth for any order k .

To summarize, the linear program that needs to be solved to find a perfectly nulling apodizing pupil mask is defined by

0. A figure of merit (FOM) which depends on the desired properties of the coronagraph,
and by the set of constraints that ensure:

1. Lyot plane nulling (equations 10, 11, or 12)

2. Feasibility (equation 13)

3. Continuity (equation 14) (optionally)

4. Smoothness (equation 15) (optionally).

The FOM used to design a PAVC depends on both instrument performance goals and how the apodization function is being produced. One of the key features of the PAVC is that it can be optimized according to different combinations of FOM and constraints. For a PAVC with a classical apodizing filter, the FOM ought to maximize filter transmission, while the smoothness and continuity constraints may be relaxed. Meanwhile, for a PAVC with shaped mirrors, a FOM must be selected that minimizes mirror curvature. In the following sections, we motivate the FOMs for PAVCs produced with either apodizing filters or with shaped mirrors, and demonstrate the results we obtain for a range of central obscuration sizes.

4. THE APODIZING FILTER PAVC

We present perfectly nulling classical apodizing masks that maximize the transmission through the mask,

$$T = \int_{R_I}^{R_P} A(r) r dr. \quad (16)$$

We only integrate the FOM T between R_I and R_P since light inside R_I is blocked by the inner Lyot stop. For a charge 2 PAVC, maximizing T is equivalent to maximizing total energy throughput² (i.e. the maximum recoverable throughput in the Lyot plane for an off-axis source), since only the a_0 and b_0 terms do not cancel out in the region $R_I < r < R_P$. This will not be the case for higher charges; however, maximizing T for $c > 2$ vortex coronagraphs will approximately maximize the throughput while allowing us to keep the problem linearized. Furthermore, maximizing transmission instead of throughput is a commonly used method to linearize problems involving optimizing apodized coronagraph design (Vanderbei et al. 2003; Carlotti et al. 2012; N'Diaye et al. 2015).

We generate optimal smooth apodizing masks for charge 2, 4, and 6 vortices described by various orders of polynomial, for different sized central obscurations. We also generate non-continuous apodizing masks, that is,

² We emphasize that T is not the same quantity as total energy throughput, which is a non-linear function of the apodization.

masks for which conditions 3 and 4 in § 2.2 have been relaxed. Profiles of smooth masks for charge 2 through 6 PAVCs are shown in Figure 2 for a pupil obscured by a secondary mirror such that $R_S = 0.3R_P$.

The total energy throughput (defined as the integrated energy in the Lyot plane that is transmitted through the pupil apodizing filter and inner Lyot stop)³ achieved by our linear programming algorithm as a function of the secondary mirror radius is shown in Figure 3, where for each R_S we chose the value of R_I that maximizes T . We find that the non-continuous apodizations have the highest throughputs for each charge, and that the smooth apodizations approach the throughput of the non-continuous apodization for a given charge as the order of the smooth piecewise polynomial increases.

Without continuity and smoothness constraints, we recover the apodization function for the charge 2 RAVC. This is not surprising, since Equation 10 constrains the portion of the apodization function where $r > R_I$ to be flat. The smooth apodization functions approach the optimal throughput for a given secondary mirror radius as the order of the polynomials used to describe the apodization function increases. For higher charges, we find apodization functions with substantially higher throughputs than those presented in Mawet et al. (2013). This is because for higher charges, the apodization function at $r > R_I$ can be expressed by progressively higher orders of polynomial, which also explains why the throughput curve for the charge 6 vortex is not perfectly monotonic—while transmission approximates throughput, the approximation is better for lower charges. Therefore, the actual best possible throughputs for a charge 4 or 6 coronagraph may be slightly higher than what we report.

To find the maximum total energy throughput achievable by a charge 4 or higher PAVC for a given R_S , one would have to use a non-linear optimizer rather than the linear programming routine we use here. However, as we will discuss in § 6, choosing the definition of throughput for optimal instrument design is non-trivial, and may depend on whether or how the PAVC is paired with a technique for compensating for struts and primary mirror segment gaps. For the purposes of demonstrating the characteristics of the PAVC, the approximate optimal total energy throughput curves we obtain by optimizing for T suffice.

Total energy throughput as a function of both secondary mirror radius and inner Lyot stop radius is shown in Figure 4. We find that the total energy throughput as a function of secondary mirror and inner Lyot stop radius increases as a function of charge. For the charge 2 coronagraph, the inner Lyot stop radius that provides the highest total throughput increases as a function of the secondary mirror radius, while the dependence of optimal inner Lyot stop radius on secondary mirror radius is more complicated for the charge 4 and 6 cases. Indeed, the throughput surface for the charge 6 coronagraph exhibits a saddle point at around $R_S/R_P = 0.3$ and $R_I/R_P = 0.4$, owing to the competing effects of loss of throughput due to increased Lyot stop size and gains

in the apodizing mask transmission. Like the result that PAVC throughput improves as charge increases, the behavior of the charge 4 and 6 throughput surfaces results from the increasing number of available degrees of freedom at $r > R_I$ as the charge increases. This is true whether or not the PAVC apodization is constrained to be smooth. As shown in Figure 4, forcing the apodization to be smooth affects the performance of the PAVC, but throughputs for both smooth and discontinuous apodizations are similar and depend on R_S and R_I in nearly the same way.

Off-axis source throughput for smooth masks designed for central obscurations with radii of $0.1R_P$ and $0.3R_P$ are shown in Figure 5. We assume the off-axis source is a faint point source, such as an exoplanet. We plot the total energy off-axis throughput (the total energy of the off-axis source in the Lyot plane relative to what would be observed by the telescope without either a coronagraph or an on-axis point source), along with the encircled energy throughput (the relative total energy in a photometric aperture of width $0.7\lambda/D$ located on the source position in the final image plane). The encircled energy throughput is an estimate of the throughput for an off-axis source that can be recovered with aperture photometry in the image plane (Ruane et al. 2016).

In the charge 2 and 4 plots, the encircled energy throughput curves of the charge 2 and 4 RAVC are shown for reference. The smooth charge 2 PAVC underperforms the charge 2 RAVC in terms of throughput, since the ideal charge 2 apodized vortex coronagraph is the RAVC. In fact, when we optimize the smooth charge 2 PAVC, the apodization function we obtain approximates the RAVC, which can be seen in Figure 2. However, the situation is the reverse for the charge 4 PAVC, especially for the $0.3R_P$ central obscuration. In that case the smooth PAVC outperforms the off-axis throughput of the RAVC by a factor of 3. We do not show RAVC curves on our charge 6 plots, since in Mawet et al. (2013), charge > 4 RAVCs were not discussed due to low total energy throughput performance.

The choice of either a charge 4 or charge 6 PAVC for a given telescope depends on the size of the secondary mirror and whether a higher throughput or smaller effective IWA is more important. By being able to provide encircled energy throughputs of $\sim 22\%$ for an $0.3R_P$ central obscuration and $\sim 50\%$ for an $0.1R_P$ central obscuration with a charge 4 vortex ($\sim 50\%$ and $\sim 52\%$ for with a charge 6 vortex), the charge 4 and charge 6 PAVC will be capable of effectively imaging off-axis sources. While going from an $0.1R_P$ central obscuration to an $0.3R_P$ central obscuration reduces the encircled energy throughput for an off-axis source by a little more than half for the charge 4 PAVC, for the charge 6 PAVC the maximum off-axis throughput is essentially unchanged. Furthermore, going from a central obscuration of $0.1R_P$ to $0.3R_P$ the angular separation at which the encircled energy throughput reaches 20% increases from $\sim 3.5 \lambda/D$ to $\sim 4.25 \lambda/D$ for the charge 6 PAVC. By comparison, the charge 4 PAVC with a central obscuration of $0.1R_P$ obtains a 20% encircled energy throughput at an angular separation of $\sim 2.0 \lambda/D$. The charge 6 PAVC addresses the issue of throughput performance for coronagraphs designed for telescopes with large secondary mirrors. The charge 4 PAVC, meanwhile, represents a trade-off be-

³ Several definitions of “throughput” are used throughout the text, and defined as needed. We summarize these definitions in Appendix B.

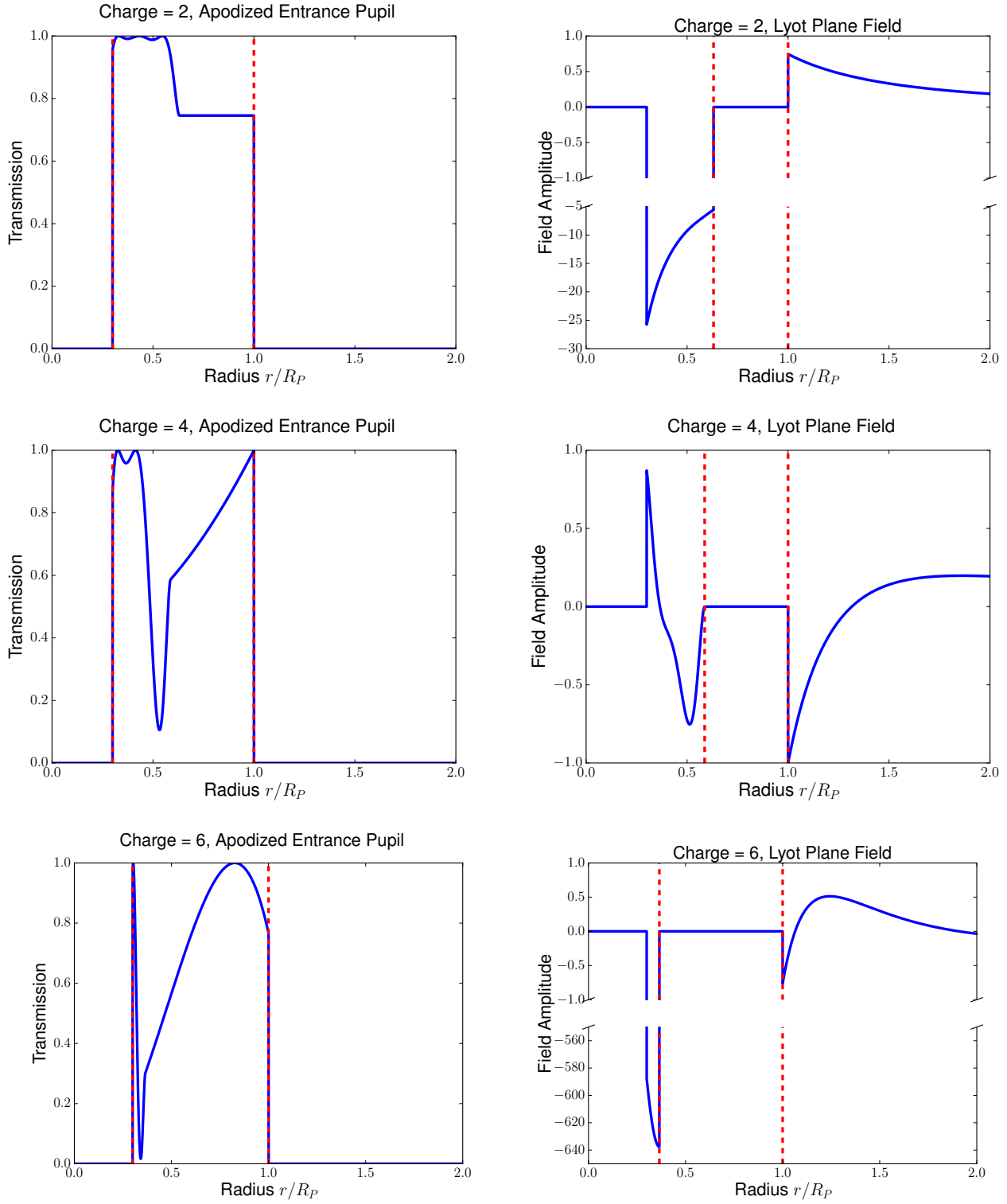


FIG. 2.— *Top Row:* The left-hand plot depicts the optimal smooth apodizing mask geometry for a coronagraph designed with a charge 2 vortex for a telescope with $R_S = 0.3R_P$. Dashed red lines depict the secondary and primary mirror radii. The right-hand panel depicts the Lyot field going out to a radius of twice the radius of the pupil. Dashed red lines depict the inner Lyot stop and pupil radii. *Middle Row:* The same set of plots are shown as in the above row, this time for a coronagraph designed with a charge 4 vortex. *Bottom Row:* The same set of plots are shown as in the above two rows, but for a charge 6 vortex.

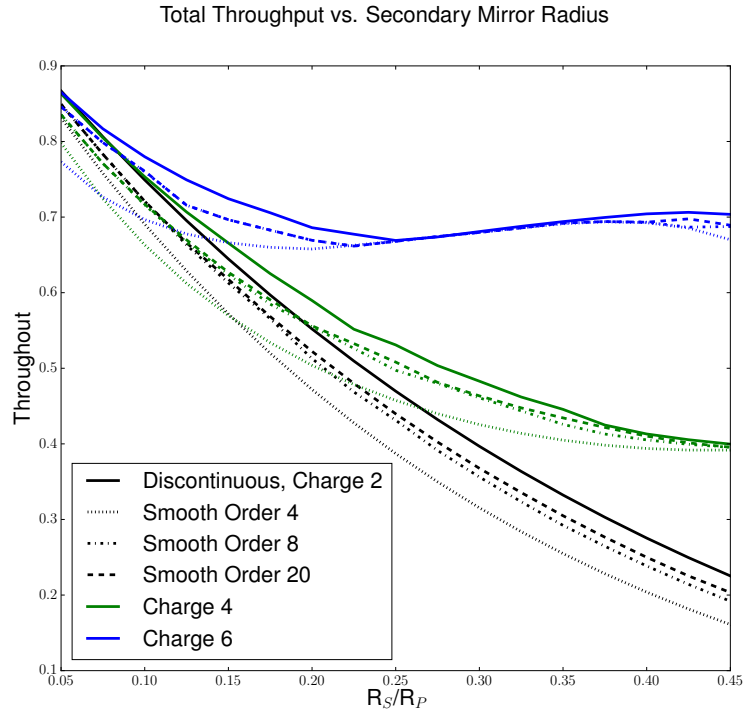


FIG. 3.— Throughput of charge 2, 4, and 6 apodized vortex coronagraphs are shown as a function of the secondary mirror radius relative to the primary mirror radius, where an apodizing filter is used. Solid curves are for apodizations that are not required to be smooth, while dotted, dash-dotted, and dashed lines are for smooth apodizations described by polynomials of order 4, 8, and 20. The black curves are for a $c = 2$ coronagraph, and the black solid line corresponds to the ring-apodized vortex coronagraph. The green curves are for a $c = 4$ coronagraph, and the blue curves are for a $c = 6$ coronagraph.

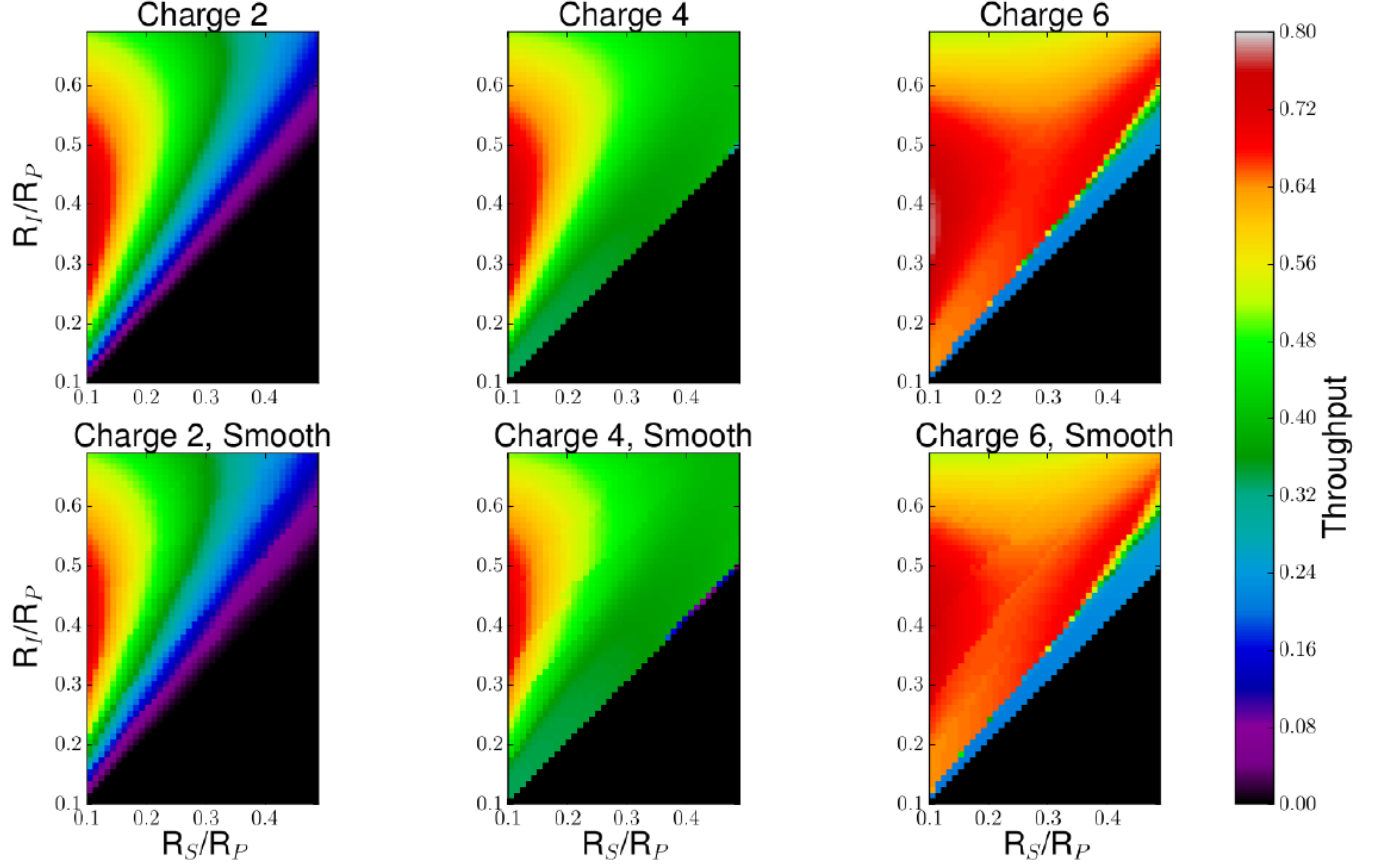


FIG. 4.— *Top Row:* Throughputs of apodizing masks optimized to maximize transmission for combinations of inner Lyot stop radius R_I and secondary mirror radius R_S for charge 2, 4, and 6 vortex phase masks. Results are shown for discontinuous apodizations. R_I and R_S are shown in units relative to the primary mirror radius, R_P . Throughput for coronagraph designs where $R_S > R_I$ are 0. *Bottom Row:* Results for smooth apodizations described by order-20 polynomials.

tween sensitivity to central obscuration size and inner working angle.

5. THE SHAPED MIRROR PAVC

We now show how smooth apodizations that null the effects of a central obscuration may be implemented with shaped mirrors. In essence, we are combining the vortex coronagraph with PIAA shaped mirror apodization, except that the shapes of the mirrors and apodizations we use differ significantly from those in Guyon et al. (2014). We modify the coronagraph design slightly, replacing the apodizing filter in Figure 1 with a pair of shaped mirrors, as shown in Figure 6. By reshaping the pupil with mirrors, instead of apodizing with a filter, there is no loss of flux due to transmission through the filter, and throughput is limited by the size of the Lyot stop. Here, we calculate the mirror shapes needed for PAVC apodization and describe the tradeoff between the coronagraph’s throughput and mirror curvature. We find mirror shapes that produce apodizations for a charge 4 and charge 6 PAVC.

We obtain expressions for circularly symmetric mirror shapes following the derivation given in Vanderbei & Traub (2005) (V05), with some modifications. A pair of mirrors is used to produce a desired apodization function—the first mirror ‘spreads out’ the incoming

point source flux, and the second mirror re-collimates the beam. We describe the shape of the first mirror with coordinates (r, θ) and mirror height (relative to a flat mirror) $h(r, \theta)$. For the second mirror we use coordinates (\tilde{r}, θ) and height $\tilde{h}(\tilde{r}, \theta)$. We drop the θ dependence throughout, since the functions we wish to solve for are circularly symmetric, and note that the more general expressions may be found in V05.

To solve for the mirror heights, we use Equations 24, 29⁴, and 34 in V05, which, dropping the θ dependence and other constants, are

$$\partial_{\tilde{r}} \tilde{h} = r(\tilde{r}) - \tilde{r}, \quad (17)$$

$$h(r) = \tilde{h}(\tilde{r}) + \frac{1}{2}(\tilde{r} - r)^2, \quad (18)$$

and

$$\frac{d}{d\tilde{r}} r(\tilde{r})^2 = 2NA^2(\tilde{r})\tilde{r}. \quad (19)$$

The extra coefficient N in Equation 19 normalizes the apodization function, so that energy is conserved across

⁴ There is a sign error in equation 29 of V05, which reads $H(r, \theta) = \tilde{H}(\tilde{r}, \theta) - \frac{P_0}{2} - \frac{(\tilde{r}-r)^2 + 2(\tilde{r}-r)\delta \cos(\theta) + \delta^2}{2P_0}$, but ought to read $H(r, \theta) = \tilde{H}(\tilde{r}, \theta) - \frac{P_0}{2} + \frac{(\tilde{r}-r)^2 + 2(\tilde{r}-r)\delta \cos(\theta) + \delta^2}{2P_0}$

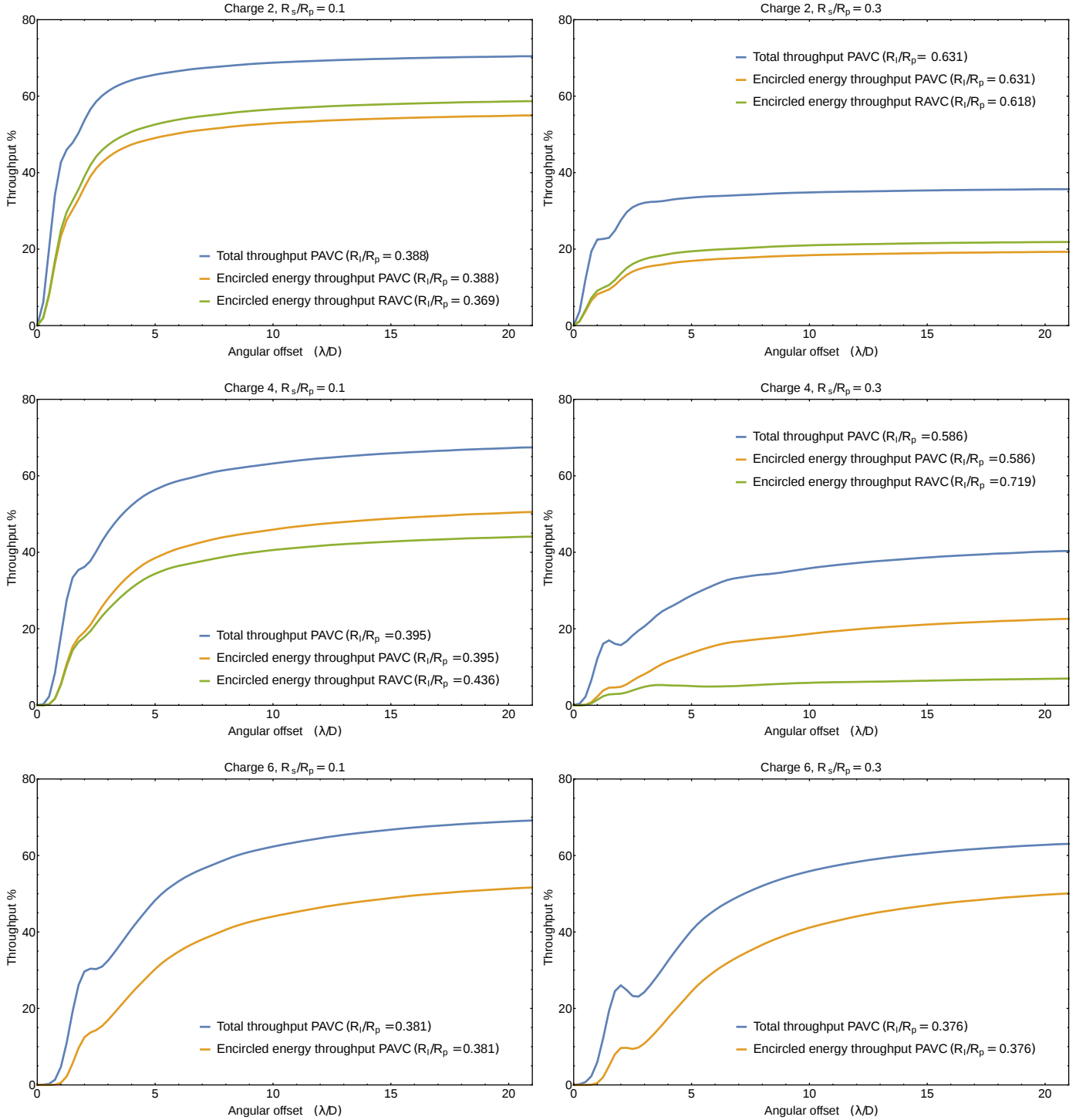


FIG. 5.— *First Row:* Off-axis throughputs for optimal coronagraph designs with a charge 2 vortex. The left-hand panel shows the throughput of an off-axis source, such as a planet, as a function of distance from the on-axis star in units of λ/D for a coronagraph designed for a telescope with $R_S = 0.1R_P$. The blue line is the total throughput, and the yellow line is the encircled energy throughput. For comparison, the green line shows the encircled energy throughput of the charge 2 RAVC for the same set of curves, this time for a coronagraph designed for a telescope with $R_S = 0.3R_P$. *Middle Row:* The same set of plots as the top row, but for a coronagraph designed with a charge 4 vortex. *Bottom Row:* The same set of plots as the top two rows, but for a coronagraph designed with a charge 6 vortex. An RAVC comparison curve is not shown, since the charge 6 RAVC was not considered in Mawet et al. (2013), owing to its low throughput.

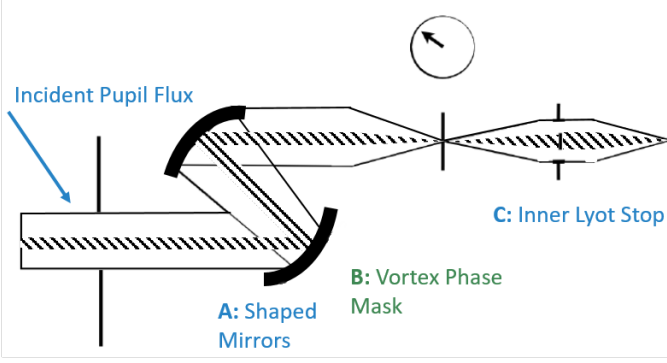


FIG. 6.— The coronagraph design from Figure 1 modified to replace the pupil plane apodizer with a pair of shaped mirrors. The shaped mirrors remap the on-axis flux to have the pupil geometry necessary to null the Lyot field. As in Figure 1, parts of the beam labeled in blue are in the pupil plane and those in green are in the focal plane.

the two mirrors, such that

$$2\pi N \int_0^{R_P} A^2(r) r dr = 2\pi R_P^2. \quad (20)$$

In order to solve Equation 19, we set $A(\tilde{r}) = 1$ for $\tilde{r} < R_S - \epsilon$, and use spline interpolation to smoothly connect $A(R_S)$ and $A(R_S - \epsilon)$, where ϵ is an arbitrary small separation. We note that it can be shown from the expression for $r(\tilde{r})$ that the equation for the derivative of the second mirror is equivalent to the second-order Monge Ampere equation for the second mirror shape presented in Pueyo et al. (2011) and Pueyo & Norman (2013).

The quantities we wish to maximize when optimizing apodizations obtained with mirror shapes are the mirrors' radii of curvature. We seek to maximize radii of curvature since mirror shapes with sharper curvatures are both more difficult to manufacture and increase the magnitude of diffraction effects introduced by the optics (Pluzhnik et al. 2006). We focus on the shape of the first mirror, which we empirically observe has the sharpest curvatures. The radius of curvature (reciprocal of the curvature, K) for this mirror is

$$\frac{1}{K} = \frac{(1 + (\partial_r h)^2)^{3/2}}{|\partial_r^2 h|}. \quad (21)$$

Finding $\partial_r h$ and $\partial_r^2 h$ is difficult using the setup described in V05, so we solve for the setup in reverse, where an incident flux with electric field amplitude $A(\tilde{r})$ is reshaped by a series of mirror to an outgoing beam of uniform amplitude. In this setup, $h(r)$ is the height of the second mirror, and the desired apodization function is $A^{-1}(r)$. Making these adjustments to Equations 17 and 18, we find that

$$\frac{1}{K} = \frac{A^2 \left(1 + \left(\frac{2}{A} - r\right)^2\right)^{3/2}}{2\partial_r A}. \quad (22)$$

To maximize the radius of curvature across the mirror shape, it follows that we want to maximize A and minimize $\partial_r A$. However, as seen in Figure 7, the minimum

value of $A(r)$ depends on R_I , which in turn sets the coronagraph total energy throughput. For a desired level of throughput, then, we can optimize for curvature by adopting $\partial_r A$ as the FOM and minimizing it.

Mirror shapes for a charge 4 coronagraph are shown in Figure 8 for $R_S = 0.1R_P$ and $R_S = 0.3R_P$. Mirrors for corresponding setups with a charge 6 vortex are shown in Figure 9. Since the beam at the pupil is reshaped by mirror shapes that are normalized to conserve energy, the total energy throughputs of these designs are calculated by

$$T_r = \frac{\pi (R_P^2 - R_I^2)}{\pi (R_P^2 - R_S^2)}. \quad (23)$$

For the charge 4 PAVCs in Figure 8, the total energy throughput is 88% for $R_S = 0.1R_P$ and 68% for $R_S = 0.3R_P$. For the charge 6 PAVCs throughputs are 86% and 88%, respectively.

The off-axis throughput curves for shaped-mirror PAVCs are shown in Figure 10. Total energy throughputs are shown as blue curves, and demonstrate a gain in throughput over the use of a greyscale apodizer for each combination of charge and secondary mirror radius we examined. Encircled energy throughputs are denoted by yellow curves. For each shaped-mirror PAVC, except for the charge 4 vortex with secondary mirror radius $R_S/R_P = 0.1$, the mirror shapes we calculate severely distort the off-axis PSF and result in a narrow range of angular separations from the on-axis star where even a modest encircled energy throughput is obtainable. Therefore, we propose using inverse mirrors placed after the Lyot stop in Stage C in Figure 6, similar to the inverse optics proposed for PIAA mirrors (Guyon et al. 2005, 2014). Our estimate of the encircled energy throughput of the restored off-axis PSF is shown by the green curve for each coronagraph design in Figure 10.

We estimated restored off-axis PSFs by propagating the off-axis point source flux through coronagraphic setups with Stage A in Figure 6 removed, and with the total energy normalized by the total energy in the final image plane of the apodized coronagraph. The restored encir-

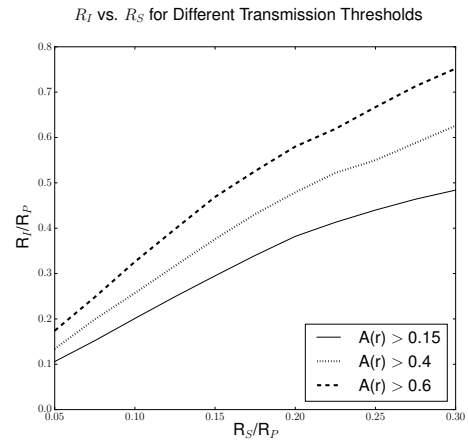


FIG. 7.— Minimum inner Lyot stop radii allowing for minimum values of $A(r)$ of 0.15 (solid lines), 0.4 (dotted), and 0.6 (dashed) are shown as a function of secondary mirror radius. For simplicity of the figure, only curves for charge 4 are shown.

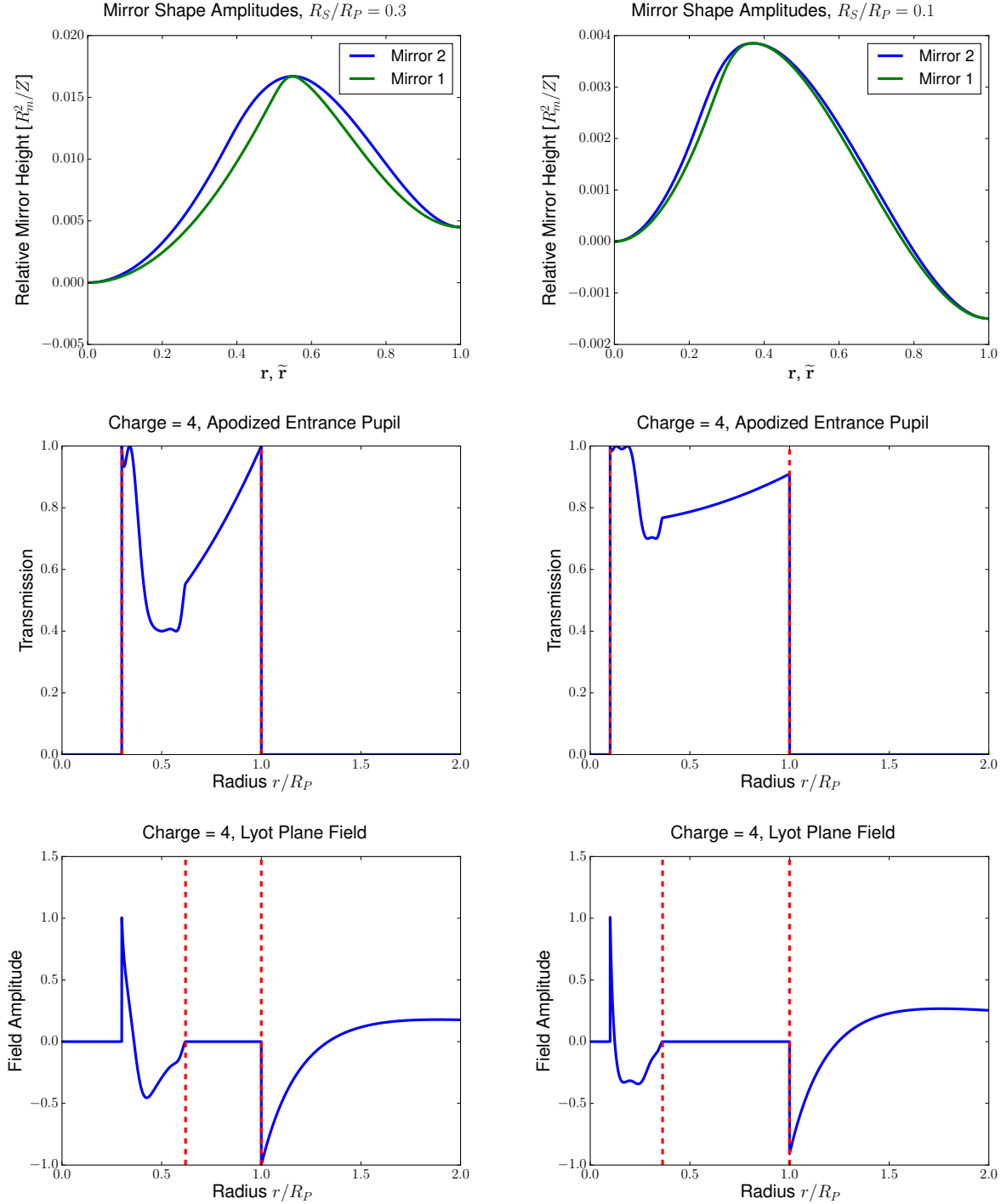


FIG. 8.— Mirror shape pairs are presented for a charge 4 PAVC for $R_S = 0.3R_P$ (left) and $R_S = 0.1R_P$ (right). Mirror shapes are on the top row, and the overall height displacement of the shapes is relative to the sizes and separation of the mirrors. Physical mirror heights depend on the radii of the shaped mirrors R_m and the separation Z between the two and go as R_m^2/Z , and translating the relative heights to a physical mirror shape involves multiplying by this factor (Traub & Vanderbei 2003; Pueyo et al. 2011; Pueyo & Norman 2013). The apodizations produced by these pairs are shown in the second row, with dashed red lines denoting the radii of the central obscuration and the pupil. The nulled field in the Lyot plane (before the inner Lyot stop) is shown in the third row, with dashed red lines denoting the inner Lyot stop and pupil radii.

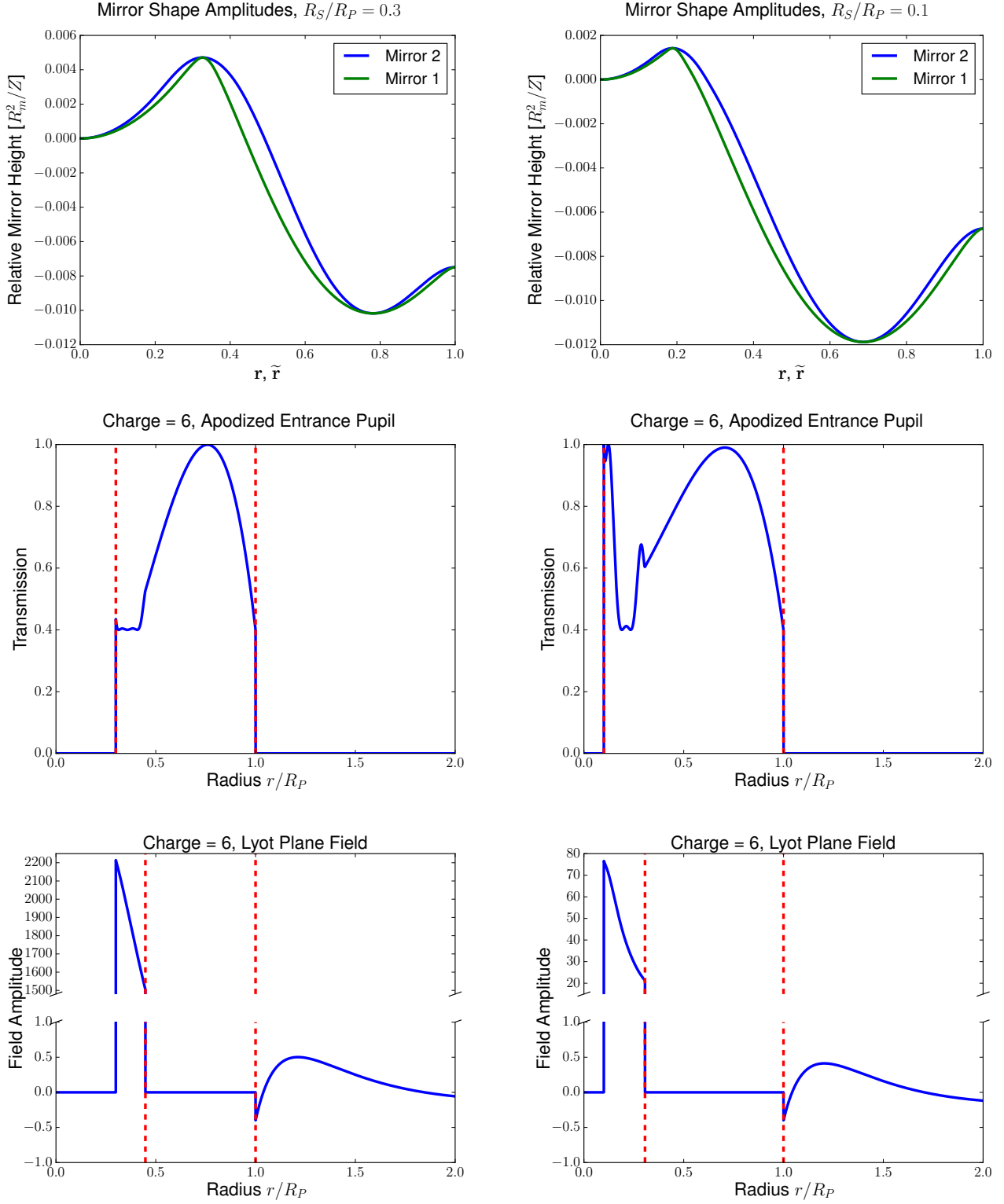


FIG. 9.— The same as Figure 8, except for a charge 6 PAVC for $R_S = 0.3R_P$ and $R_S = 0.1R_P$.

cled energy throughputs we present are therefore upper limits on what may be achieved with inverse optics. If we treat the encircled energy throughput of an off-axis source as the best estimate for the throughput of ‘usable’ photometric flux, then using shaped mirrors with inverse optics improves the performance of the charge 4 PAVC by a factor of 2 and the charge 6 PAVC by about 50%.

6. DISCUSSION

We have presented a linear algorithm that optimizes charge 2, 4, and 6 polynomial apodized vortex coronagraphs that entirely null the flux due to an on-axis point source. The apodization functions we derive offer throughputs that are competitive with or substantially higher than other high-contrast coronagraph designs (e.g. Mawet et al. (2013); N’Diaye et al. (2015); Guyon et al. (2014)) for centrally obscured pupils, and are achromatic by virtue of nulling the electric field in the Lyot plane. This apodization prescription is especially useful with charge 4 and 6 vortices. Since the number of degrees of freedom describing the apodization function at $r > R_I$ increases with charge, the maximum attainable throughput increases as a function of charge, and drops as a function of R_S more gradually as charge increases as well. Furthermore, the possibility of using shaped mirrors allows us to consider coronagraph designs with total energy throughputs determined by the size of the inner Lyot stop alone.

The analytical prescription we derived for the PAVC overcomes a fundamental hurdle associated with the vortex coronagraph—the loss of starlight suppression due to the obscuration created by the secondary mirrors of on-axis telescopes. With the apodizing pupil masks in this paper, we are able to restore the theoretically ideal starlight suppression of the vortex coronagraph while maintaining off-axis throughput. In combination with techniques for minimizing the impact of pupil features imposed by secondary mirror support struts and primary mirror segmentation gaps, our solution enables vortex coronagraphs to be used with the complex apertures of future space and ground based large-aperture on-axis telescopes.

Recently, numerical algorithms have been put forward to calculate either apodizing mask or shaped mirror geometries that mitigate the effects of struts and primary mirror gaps (so-called ‘spiders’) on vortex coronagraph starlight suppression (Ruane et al. 2016; Mazoyer et al. 2015, 2016). By using a PAVC apodizer to correct for the central obscuration, we are able to provide a first order correction for the vortex coronagraph on an obstructed pupil. Higher order corrections to the PSF can then be obtained using either e.g. Ruane et al. (2016) or Mazoyer et al. (2016) to create a dark hole with $\sim 10^{-10}$ contrast while minimizing losses to throughput.

Figure 11 depicts an example of how a such a combined approach works on obstructed pupil with a central obscuration of radius $R_S/R_P = 0.17$ and segment gaps. The pupil shown in Figure 11 is a realistic aperture for future space telescope missions taken from the Segmented Coronagraph Design and Analysis (SCDA) program.⁵ Using a charge 6 PAVC with an inner Lyot stop of radius $R_I = 0.414R_P$, we correct for the central

obscuration. In the absence of spiders, this configuration of polynomial apodized vortex coronagraph provides ideal on-axis point source suppression and an encircled energy throughput of 44%. However, in the presence of segment gaps in this pupil, the contrast is reduced to 10^{-6} assuming broadband light with a 30% bandwidth.

We combine this apodizing filter with mirror shapes obtained using the ACAD-OSM (Active Correction of Aperture Discontinuities- Optimized Stroke Minimization) algorithm in Mazoyer et al. (2016), shown in Figure 11. The shaped mirror corrections provide a PSF with a dark hole between 1.5 and 15 λ/D providing a contrast of 10^{-10} in 30% bandwidth light. Encircled energy throughput of an off-axis point source as a function of angular separation from the star is shown in Figure 12. The additional correction to the pupil geometry provided by the shaped mirrors reduces encircled energy throughput; however, the encircled energy throughput in the dark hole exceeds 20% at 4.5 λ/D . At the outer edge of the dark hole, where throughput is highest, this rises to $\sim 41\%$.

The example coronagraph design discussed here may be optimized substantially depending on demands imposed on the coronagraph by the initial pupil geometry. In particular, throughput of the spider correction depends heavily on the inner Lyot stop radius used, and it may be possible to determine an ideal inner Lyot stop radius for a combination of polynomial apodizing filter and spider-correcting apodization. Furthermore, polynomial apodizing geometries that correct for the central obscuration may also be optimized to result in a pupil geometry that requires less correction with numerical techniques. In the present discussion, we have presented proof of concept for this configuration of apodized vortex coronagraph.

Currently, we are working on extending our technique for deriving PAVC apodizations to analytically describe impacts of low-order aberrations on PAVC designs, and to optimize the PAVC to minimize sensitivity to these effects. With an unobstructed circular aperture, the sensitivity of a vortex coronagraph to small angular offsets of the on axis source caused by low order aberrations goes approximately as s^c , where s is the size of the offset and c is the charge of the vortex (Jenkins 2008; Mawet et al. 2010). Therefore, as the charge of a vortex coronagraph increases, the coronagraph becomes more robust to low-order aberrations. However, in the presence of a central obscuration, vortex coronagraphs are less robust to these aberrations for a given charge, and the flux ‘leak’ caused by small angular offsets rises more steeply than s^c . Since the PAVC allows for high-throughput coronagraphs be constructed for on-axis telescopes with charge 4 and 6 vortices, addressing this issue of robustness will allow the PAVC to take advantage of the stability of these charges relative to the charge 2 vortex, as well as their relative insensitivity to finite stellar angular size.

Finally, we briefly discuss the issue of the FOM used to design the PAVC with classical apodizing filters. As discussed in § 4, we calculated PAVC apodizations by maximizing transmission of the apodizing filter, which is a linear quantity that approximates throughput. However, the actual quantity that determines the relative flux from an exoplanet or other off-axis source that the ob-

⁵ https://exoplanets.nasa.gov/system/internal_resources/details/original/211_SCDAApertureDocument050416.pdf

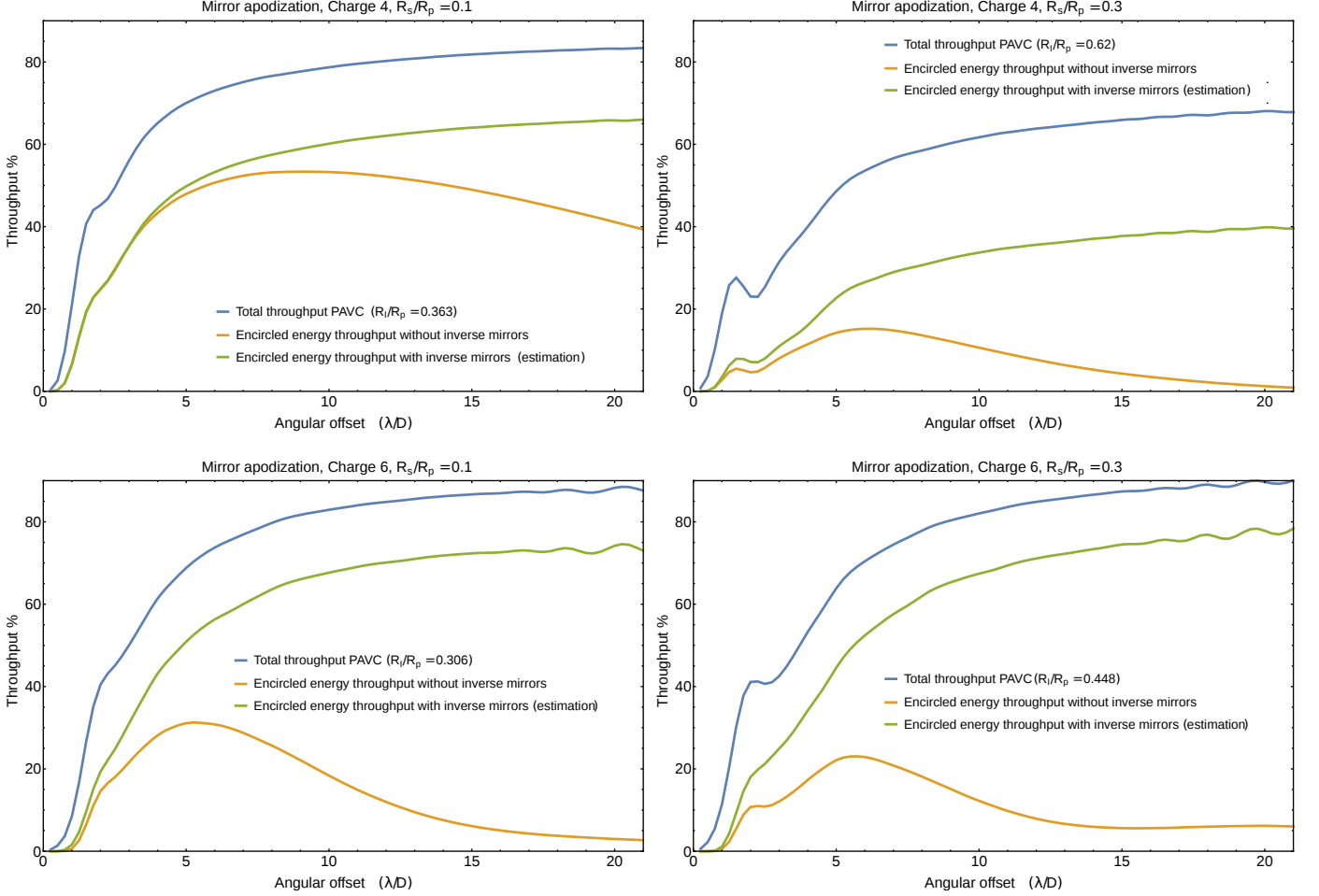


FIG. 10.— *Top Row:* Off-axis throughputs for optimal coronagraph designs with a charge 4 PAVC, where apodizations were obtained with shaped mirrors. The left-hand panel shows the throughput of an off-axis source, as a function of distance from the on-axis star in units of λ/D for a coronagraph designed for a telescope with $R_S = 0.1R_P$. The blue line is the total throughput, and the yellow line is the encircled energy throughput. The green line depicts the approximate encircled energy throughput obtained when the off-axis PSF is restored by inverse mirrors placed after the Lyot plane. The right-hand panel show the same set of curves, this time for a coronagraph designed for a telescope with $R_S = 0.3R_P$. *Bottom Row:* The same set of plots as the top two rows, but for a coronagraph designed with a charge 6 vortex.

server will be able to detect is best approximated by the encircled energy throughput shown in Figures 5 and 10. Since the encircled energy throughput is a function of angular separation, the optimal FOM will depend on performance goals for effective inner working angle as well as overall throughput. For example, the optimal FOM for a given coronagraph may be the encircled energy throughput at $3 \lambda/D$. The situation is more complicated though, since vortex coronagraphs designed for complex on-axis telescope pupil will need to combine the PAVC with a technique for compensating for spiders. Therefore, applications of the PAVC to obstructed pupils will likely involve a FOM that takes into account the encircled energy throughput at a given angular separation of a combined PAVC + spider-correcting apodization design. Such a FOM will require us to adopt a non-linear algorithm for optimizing the pupil apodization. Fortunately, since PAVC designs have a large number of degrees of freedom and few constraints to ensure ideal starlight suppression, they are well-suited to addressing complex optimization problems.

7. CONCLUSION

In this paper, we derived the analytical expression for the propagation of centrally obscured, apodized pupils through a vortex phase mask by deriving the centrally obscured vortex operator for charge 2, 4, and 6 vortex coronagraphs. We then used these results to find polynomial apodized vortex coronagraphs (PAVCs) that provide theoretically perfect on-axis starlight suppression. We calculated both smooth and discontinuous classically apodizing masks for charge 2, 4, and 6 coronagraphs that optimize coronagraphic transmission. These PAVC designs have total energy throughputs (relative to a centrally obscured telescope with no coronagraph) of $\sim 75\%$, 75% , and 80% for charges 2-6 respectively with a central obscuration with $R_S = 0.1R_P$, and $\sim 35\%$, 45% , and 70% with a central obscuration with $R_S = 0.3R_P$. We found that overall throughput is a decreasing function of the size of the central obscuration. However, unlike with the RAVC, for the family of apodizations we found the throughput increases with the charge of the vortex mask, and decreases more slowly for progressively larger central

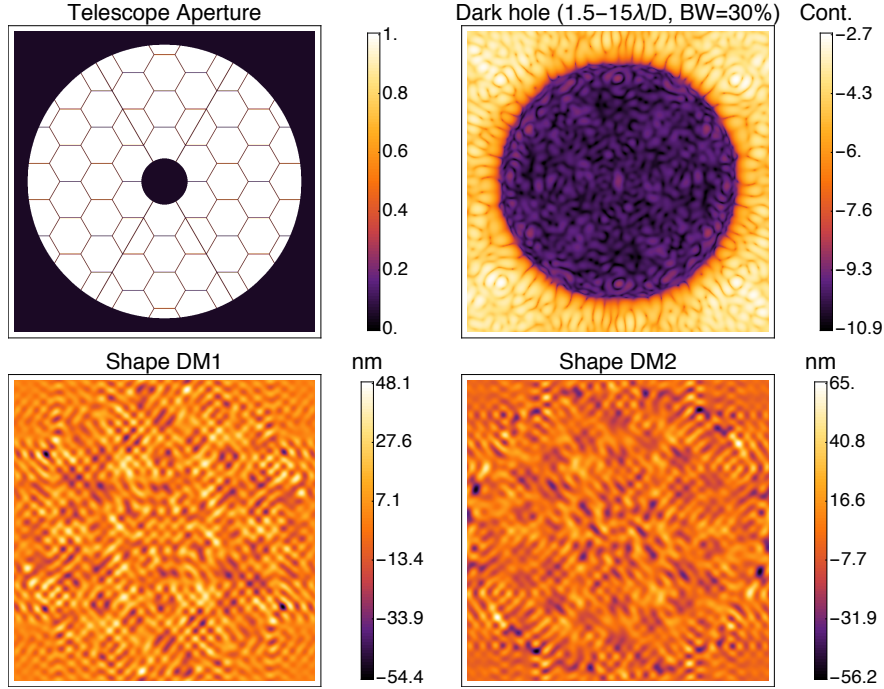


FIG. 11.— An example deformable mirror solution that creates a dark hole PSF for a centrally obstructed aperture in conjunction with a polynomial apodizing mask. The pupil, featuring a secondary mirror obscuration with $R_S/R_P = 0.17$ and segment gaps is shown in the upper left. The lower left and lower right show the mirror shapes that provide the higher-order correction for segment gaps using ACAD-OSM (Mazoyer et al. 2016) and, in conjunction with an apodizing mask, produce the PSF in the upper right. The PSF features a dark hole with a contrast of approximately 10^{-10} in the region $1.5 - 15 \lambda/D$.

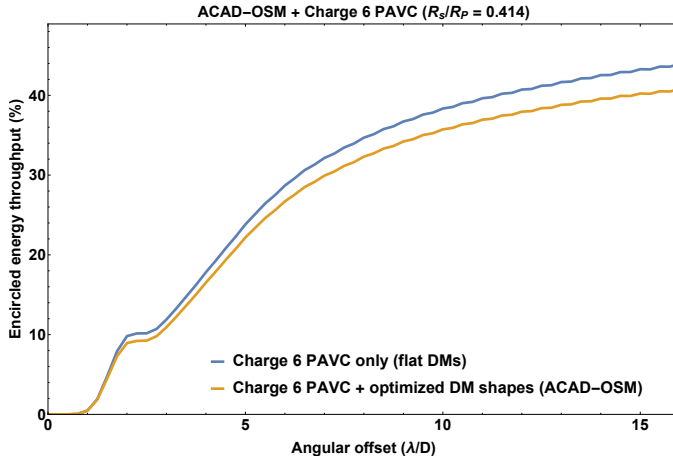


FIG. 12.— Encircled energy throughput vs. offset for a polynomial apodized + ACAD-OSM vortex coronagraph design. The blue curve shows the throughput obtained in the absence of mirror deformations, while the purple curve shows the throughput obtained when both a polynomial apodizer and shaped mirrors are used to correct the central obscuration and segment gaps.

obscurations. For a central obscuration of $R_S = 0.3R_P$, the ‘encircled energy’ throughput, which approximates the throughput on the signal which would be recovered via aperture photometry, is $\sim 22\%$ for a charge 4 PAVC, dropping from $\sim 50\%$ for $R_S = 0.1R_P$ and $\sim 50\%$ for a charge 6 PAVC, dropping barely at all.

Since mask geometries can be constrained to be smooth, we also explored the possibility of producing apodizing masks with pairs of shaped mirrors. The radius of curvature of the first mirror depends both on the inner Lyot stop (and therefore the instrument throughput) of the coronagraph and the inverse of the first derivative of the apodization function. We presented pairs of mirror shapes that maximize the radius of curvature by minimizing $\partial_r A(r)$ given a secondary mirror radius and inner Lyot stop radius for a charge 4 and a charge 6 PAVC. While these throughput-maximizing results produced mirror shapes that require inverse-mirror optics to obtain useful off-axis PSFs, our algorithm can also be used to find the trade-off between throughput and curvature that may allow us to overcome the limitation imposed by off-axis PSF distortion by the shaped mirrors.

Our results overcome the challenge posed by large cen-

tral obscurations for the use of vortex coronagraphs with on-axis telescopes. We describe a family of analytically derived apodizing pupil masks that restore ideal starlight suppression, while preserving high throughputs for off-axis sources for coronagraphs with vortex charges > 2 . These results allow us to design charge 4 and 6 vortex coronagraphs for on-axis telescopes.

As mentioned in Ruane et al. (2016), synergy exists between apodized vortex coronagraph designs that compensate for central obscurations and designs that compensate for pupil obstructions introduced by struts and primary mirror gaps. We provide an example of implementing a synergistic PAVC + numerical design by combining the PAVC with ACAD-OSM pupil shaping

(Mazoyer et al. 2016). Our results greatly expand the flexibility of vortex coronagraph designs, and represent a step forward towards implementing vortex coronagraphs capable of directly imaging Earth sized exoplanets.

ACKNOWLEDGMENTS

We acknowledge discussions with Garreth Ruane and Dimitri Mawet that helped enhance our discussion on combining the PAVC with numerical apodization techniques to design coronagraphs for telescopes with pupils that feature both central obscurations and ‘spiders.’ This material is partially based upon work carried out under subcontract 1496556 with the Jet Propulsion Laboratory funded by NASA and administered by the California Institute of Technology.

REFERENCES

- Andrews, S. M., Wilner, D. J., Espaillat, C., et al. 2011, *ApJ*, 732, 42
- Bolcar, M. R., Balasubramanian, K., Clampin, M., et al. 2015, in *Proc. SPIE*, Vol. 9602, Optics for EUV, X-Ray, and Gamma-Ray Astronomy VII, 960209
- Cady, E. 2012, *ApJs*, 201, 25
- Carlotti, A., Kasdin, N. J., Vanderbei, R. J., & Delorme, J.-R. 2012, in *Proc. SPIE*, Vol. 8442, Space Telescopes and Instrumentation 2012: Optical, Infrared, and Millimeter Wave, 844254
- Carson, J., Thalmann, C., Janson, M., et al. 2013, *ApJ*, 763, L32
- Dalcanton, J., Seager, S., Aigrain, S., et al. 2015, *ArXiv e-prints*, arXiv:1507.04779
- Fogarty, K., Pueyo, L., & Mawet, D. 2014, in *Proc. SPIE*, Vol. 9143, Space Telescopes and Instrumentation 2014: Optical, Infrared, and Millimeter Wave, 914326
- Foo, G., Palacios, D. M., & Swartzlander, Jr., G. A. 2005, *Optics Letters*, 30, 3308
- Guyon, O. 2003, *A&A*, 404, 379
- Guyon, O., Hinz, P. M., Cady, E., Belikov, R., & Martinache, F. 2014, *ApJ*, 780, 171
- Guyon, O., Pluzhnik, E. A., Galicher, R., et al. 2005, *ApJ*, 622, 744
- Jenkins, C. 2008, *MNRAS*, 384, 515
- Kalas, P., Graham, J. R., Chiang, E., et al. 2008, *Science*, 322, 1345
- Kasper, M., Beuzit, J.-L., Verinaud, C., et al. 2010, *EPICS: direct imaging of exoplanets with the E-ELT*, doi:10.1117/12.856850
- Kuchner, M. J., & Traub, W. A. 2002, *ApJ*, 570, 900
- Kuzuhara, M., Tamura, M., Kudo, T., et al. 2013, *ApJ*, 774, 11
- Lagrange, A.-M., Gratadour, D., Chauvin, G., et al. 2009, *A&A*, 493, L21
- Lyot, B. 1939, *MNRAS*, 99, 580
- Macintosh, B., Graham, J. R., Barman, T., et al. 2015, *Science*, 350, 64
- Mancini, L., Hartman, J. D., Penev, K., et al. 2015, *A&A*, 580, A63
- Marois, C., Macintosh, B., Barman, T., et al. 2008, *Science*, 322, 1348
- Marois, C., Zuckerman, B., Konopacky, Q. M., Macintosh, B., & Barman, T. 2010, *Nature*, 468, 1080
- Martinez, P., Dorner, C., Aller Carpentier, E., et al. 2009, *A&A*, 495, 363
- Mawet, D., Pueyo, L., Carlotti, A., et al. 2013, *ApJS*, 209, 7
- Mawet, D., Pueyo, L., Moody, D., Krist, J., & Serabyn, E. 2010, in *Society of Photo-Optical Instrumentation Engineers (SPIE) Conference Series*, Vol. 7739, Society of Photo-Optical Instrumentation Engineers (SPIE) Conference Series
- Mawet, D., Riaud, P., Absil, O., & Surdej, J. 2005, *ApJ*, 633, 1191
- Mawet, D., Riaud, P., Hanot, C., et al. 2007, in *Society of Photo-Optical Instrumentation Engineers (SPIE) Conference Series*, Vol. 6693, Society of Photo-Optical Instrumentation Engineers (SPIE) Conference Series
- Mawet, D., Serabyn, E., Wallace, J. K., & Pueyo, L. 2011a, *Optics Letters*, 36, 1506
- Mawet, D., Trauger, J. T., Serabyn, E., et al. 2009, in *Society of Photo-Optical Instrumentation Engineers (SPIE) Conference Series*, Vol. 7440, Society of Photo-Optical Instrumentation Engineers (SPIE) Conference Series
- Mawet, D., Serabyn, E., Moody, D., et al. 2011b, in *Society of Photo-Optical Instrumentation Engineers (SPIE) Conference Series*, Vol. 8151, Society of Photo-Optical Instrumentation Engineers (SPIE) Conference Series
- Mazoyer, J., Pueyo, L., N'Diaye, M., et al. 2016, in *Proc. SPIE*, Vol. 9904, Society of Photo-Optical Instrumentation Engineers (SPIE) Conference Series, 99044T
- Mazoyer, J., Pueyo, L., Norman, C., et al. 2015, in *Proc. SPIE*, Vol. 9605, Techniques and Instrumentation for Detection of Exoplanets VII, 96050M
- Moody, D. C., Gordon, B. L., & Trauger, J. T. 2008, in *Proc. SPIE*, Vol. 7010, Space Telescopes and Instrumentation 2008: Optical, Infrared, and Millimeter, 70103P
- Moody, D. C., & Trauger, J. T. 2007, in *Proc. SPIE*, Vol. 6693, Techniques and Instrumentation for Detection of Exoplanets III, 66931I
- Murakami, N., & Baba, N. 2005, *PASP*, 117, 295
- N'Diaye, M., Pueyo, L., & Soummer, R. 2015, *ApJ*, 799, 225
- Newman, K., Belikov, R., Pluzhnik, E., Balasubramanian, K., & Wilson, D. 2014, in *Proc. SPIE*, Vol. 9151, Advances in Optical and Mechanical Technologies for Telescopes and Instrumentation, 91515O
- Pluzhnik, E. A., Guyon, O., Ridgway, S. T., et al. 2006, *ApJ*, 644, 1246
- Pueyo, L., Kasdin, N. J., Carlotti, A., & Vanderbei, R. 2011, *ApJS*, 195, 25
- Pueyo, L., & Norman, C. 2013, *ApJ*, 769, 102
- Rameau, J., Chauvin, G., Lagrange, A.-M., et al. 2013, *ApJ*, 772, L15
- Rouan, D., Riaud, P., Boccaletti, A., Clénet, Y., & Labeyrie, A. 2000, *PASP*, 112, 1479
- Ruane, G., Jewell, J., Mawet, D., Pueyo, L., & Shaklan, S. 2016, *ArXiv e-prints*, arXiv:1607.06400
- Sivaramakrishnan, A., Koresko, C. D., Makidon, R. B., Berkefeld, T., & Kuchner, M. J. 2001, *ApJ*, 552, 397
- Sivaramakrishnan, A., & Yaitskova, N. 2005, *ApJ*, 626, L65
- Soummer, R. 2005, *ApJL*, 618, L161
- Soummer, R., Sivaramakrishnan, A., Pueyo, L., Macintosh, B., & Oppenheimer, B. R. 2011, *ApJ*, 729, 144
- Traub, W. A., & Vanderbei, R. J. 2003, *ApJ*, 599, 695
- Trauger, J., Moody, D., Gordon, B., Krist, J., & Mawet, D. 2012, in *Proc. SPIE*, Vol. 8442, Space Telescopes and Instrumentation 2012: Optical, Infrared, and Millimeter Wave, 84424Q
- Vanderbei, R. J., Kasdin, N. J., Spergel, D. N., & Kuchner, M. 2003, in *Proc. SPIE*, Vol. 5170, Techniques and Instrumentation for Detection of Exoplanets, ed. D. R. Coulter, 49–56
- Vanderbei, R. J., & Traub, W. A. 2005, *ApJ*, 626, 1079
- Wagner, K., Apai, D., Kasper, M., & Robberto, M. 2015, *ApJ*, 813, L2

APPENDIX
VORTEX OPERATOR FOR ANALYTICAL PUPIL SHAPES

While the central obscuration imposed by the secondary mirror is the largest feature in the pupil geometry of an on-axis telescope design, on axis designs will also feature a number of spiders. In the following, we demonstrate how the prescription we present in Section 2 for circularly symmetric pupils may be extended to describe the propagation of non-circularly symmetric components of a telescope pupil.

The vortex operator we have described in this paper may be extended for any aperture geometry that can be described by a Zernike polynomial expansion. Such a description allows us to analytically propagate the effects of both the secondary mirror of an on-axis telescope and the pupil ‘spiders’ which result from discontinuities in the primary mirror and the support structure for the secondary mirror.

We consider a pupil geometry which can be expanded into terms $r^{n_p} e^{im_p \theta}$, in the region $R_S \leq r \leq R_P$, and an apodizing mask which can be expanded into terms $r^{n_m} e^{im_m \theta}$. The apodized pupil geometry therefore consists of terms

$$r^n e^{im\theta} = (r^{n_p} e^{im_p \theta}) (r^{n_m} e^{im_m \theta}). \quad (\text{A1})$$

The electric field at the Lyot plane for a $c = 4$ coronagraph for one of these terms is analytic so long as $n + m$ is even, unless $n \geq 0$ and $n + m = -4$ or $n + m = -2$. For a given term

$$f_{n,m}(r, \theta) = \begin{cases} 0, & \text{if } r < R_i. \\ r^n e^{im\theta}, & \text{if } R_i \leq r \leq R_P \end{cases} \quad (\text{A2})$$

the electric field in the Lyot plane at $R_i \leq r \leq R_P$ is

$$V_4[f_{n,m,p}(r, \theta)] = e^{i(m+4)} [C_0(n, m) r^n + C_1(n, m) r^{-m-2} + C_2(n, m) r^{-m-4}] \quad (\text{A3})$$

where

$$C_0(n, m) = \frac{(n-m)(n-m-2)}{(n+m+4)(n+m+2)}, \quad (\text{A4})$$

$$C_1(n, m) = \frac{-2(m+1)(m+2)}{m+n+2} \begin{cases} R_i^{m+n+2}, & \text{if } m \geq -1 \\ R_P^{m+n+2}, & \text{if } m < -1, \end{cases} \quad (\text{A5})$$

and

$$C_2(n, m) = \frac{2(m+2)(m+3)}{m+n+4} \begin{cases} R_i^{m+n+4}, & \text{if } m \geq -1 \\ R_P^{m+n+4}, & \text{if } m < -1. \end{cases} \quad (\text{A6})$$

DEFINITIONS OF THROUGHPUT

Total Energy Throughput: The integrated energy in the Lyot plane of a PAVC that is transmitted through the pupil and Lyot stop. For a classically apodized PAVC, this quantity can be calculated by

$$Tr = \frac{2\pi \int_{R_I}^{R_P} A^2(r) r dr}{\pi(R_P^2 - R_S^2)}. \quad (\text{B1})$$

Total Energy Off-Axis Throughput: The total energy of an off-axis source in the Lyot plane. For a classically apodized PAVC, this quantity can be calculated by

$$Tr(r) = \frac{\int_{R_I}^{R_P} \int_0^{2\pi} (V_c[A(r)F(r, \theta)])^2 d\theta r dr}{\pi(R_P^2 - R_S^2)}, \quad (\text{B2})$$

where $F(r, \theta)$ is the off-axis source flux in the telescope pupil.

Encircled Energy Throughput: The integral of the energy contained in an aperture of diameter $0.7\lambda/D$ centered on the off-axis source position in the image plane of the PAVC. If (K_x, K_y) is the position of the off-axis source in coordinates centered on the on-axis star, then the encircled energy throughput is

$$Tr(K) = \frac{\int_{(k_x - K_x)^2 + (k_y - K_y)^2 \leq (0.35\lambda/D)^2} I^2(k_x, k_y) dk_x dk_y}{\pi(R_P^2 - R_S^2)}, \quad (\text{B3})$$

where $K \equiv \sqrt{K_x^2 + K_y^2}$ and $I(k_x, k_y)$ is the amplitude in the image plane.